# Three-Dimensional Trampolinelike Behavior in an Ultralight Elastic Metamaterial

Nikhil JRK Gerard,[1,2] Mourad Oudich,[1,2,3] Zhenpeng Xu,[4] Desheng Yao,[4] Huachen Cui,[4] Christina J. Naify,[5] Alec Ikei,[5] Charles A. Rohde,[5] Xiaoyu (Rayne) Zheng,[4,*] and Yun Jing[1,2,†]

[1] *Graduate Program in Acoustics, The Pennsylvania State University, University Park, Pennsylvania, 16802, USA*

[2] *Department of Mechanical and Aerospace Engineering, North Carolina State University, Raleigh, North Carolina 27695, USA*

[3] *Institut Jean Lamour, Université de Lorraine, CNRS, Nancy, 54000, France*

[4] *Department of Civil and Environmental Engineering and Mechanical and Aerospace Engineering, University of California, Los Angeles, California 90095, USA*

[5] *U.S. Naval Research Laboratory, Code 21760, Washington 20375, USA*

(Received 30 April 2021; revised 24 June 2021; accepted 20 July 2021; published 9 August 2021)

Elastic metamaterials possess band gaps, or frequency ranges that are forbidden to wave propagation. Existing solutions for impeding three-dimensional (3D) wave propagation largely rest on high-volume fractions of mass inclusions that induce and tailor negative effective density-based local resonances. This study introduces a class of elastic metamaterials that achieve low-frequency band gaps with a volume fraction as low as 3% (mass density as low as 0.034 g/cm$^3$). The working of the proposed design hinges on a 3D trampolinelike mode behavior that gives rise to wide, omnidirectional, and low-frequency band gaps for elastic waves despite very low-mass densities. Such a 3D trampoline effect is derived from a network of overhanging nodal microarchitectures that act as locally resonating elements, which give rise to band gaps at low frequencies. The dynamic effective properties of the metamaterial are numerically examined, which reveal that the band gap associated with the trampoline effect is resulted from a negative effective modulus coupled with a near-zero yet positive effective density. The experimental characterization is then made possible by fabricating the metamaterial via a light-based printing system that is capable of realizing microarchitectures with overhanging microfeatures. This design strategy could be useful to applications where simultaneous light weight and vibration control is desired.

DOI: 10.1103/PhysRevApplied.16.024015

## I. INTRODUCTION

Controlling wave propagations via designed structures is essential in sound attenuation and vibration mitigation. Periodic architectures potentially offer band gaps (BGs) or frequency ranges where wave propagation is forbidden. However, relying on periodic phononic crystals with Bragg scattering alone, is far from being practical in managing low-frequency vibrations as long wavelengths require impractically large features. Elastic metamaterials offer the unique advantage of controlling acoustic [1,2] and elastic waves [3,4] owing to their ability of tailoring band gaps at wavelengths much larger than their periodicities. These metamaterials are typically constructed by inserting heavy mass at the core of the periodic scaffold, which induces a local resonance phenomenon [5–15]. Via tailoring the lattice geometry and stiffness of the mass inclusions, a range of low-frequency and wide band gaps can be generated and tuned. This intuitive design concept, however, comes at the cost of significantly added masses, rendering them impractical when scaled up for engineering applications. While a few alternative methods [3,16–18] have been demonstrated based on periodic arrangement of pillars and hole arrays on a plate that achieve low-frequency band gaps, these designs are only capable of operating in the case of two-dimensional (2D) plate (Lamb) waves. Achieving three-dimensional (3D) omnidirectional low-frequency band gaps still requires large mass inclusions. Developing lightweight three-dimensional metamaterials for low-frequency vibration isolation from all directions, thus, remains elusive.

In this work, we introduce a class of ultralow density elastic metamaterials that exhibit a three-dimensional trampolinelike resonance and can achieve wide-band omnidirectional vibration attenuation at low frequencies. The high porosity (exceeding 95% void space) of our microlattice enables a mass density that is as low as 0.034 g/cm$^3$. The design features a network of low stiffness

*rayne@seas.ucla.edu
†yqj5201@psu.edu

 © 2021 American Physical Society

nodal structures within an array of overhanging microunit cells that facilitate a pair of distinct local resonance-based band gaps at relatively low frequencies. The proposed metamaterial is analyzed via a theoretical lumped model and its dynamic properties are numerically investigated to show that the 3D trampoline effect gives rise to a band gap that is associated with negative bulk modulus and near-zero yet positive effective density over a wide frequency range. This is quite different from the BGs seen in conventional 3D elastic metamaterials that rely entirely on heavy masses to induce negative effective density-based local resonances. The fabrication of the ultra-light prototype is enabled by a large area projection microstereolithography platform capable of microscale overhanging 3D features that make up the isotoxal auxetic topology of the proposed metamaterial. The observed low-frequency band gaps in these ultralow density metamaterials decouples the previous mass density and feature size trade-off for elastic metamaterials and offers insights on the dynamic behavior of microlattice-based metamaterials for applications in vibration control and energy harvesting for aerospace, automotive, and civil infrastructural systems.

## II. UNIT-CELL DESIGN

Three-dimensional architected metamaterials represent a promising class of low-density materials with microlattice topologies that offer numerous advantages in structural [19,20], thermal [21], and energy absorption [22, 23] properties. These metamaterials include octet-truss, tetrakaidecahedron, kagome, and auxetic lattices that comprise open cellular topologies with nodal connectivity that can be additively manufactured and can display high strength and tailorable energy absorption at a fraction of the weight of the solid material.

Auxetic lattices are those that exhibit a static negative Poisson ratio by counterintuitively increasing (or decreasing) in the lateral direction when they are subject to a tensile (or compressive load) [24–28]. These were put forward a couple of decades ago and have ever since been investigated for their usefulness in various biomedical, aerospace, and textile applications, owing to their compressibility and energy-absorption capabilities. Efforts have also revealed that in addition to the conventional auxetic geometries, auxeticity can also be induced via chirality [29–31], rotating units [32,33], and random or entangled topologies [33,34]. Auxetic microlattices are hence excellent candidates for multiple functionalities and some recent studies have also engineered microlattices to possess band gaps for elastic waves alongside auxeticity. However, the majority of these works are theoretical and have been constrained to 2D wave propagation [35–37], and the few designs proposed for 3D [8,38,39] still rely on heavy masses in the core of the unit cells, to induce negative density-based bandgaps. This study on the other hand, proposes a 3D auxetic microlattice that possesses a trampolinelike dynamic negative-modulus-based resonance that enables wide band gaps despite the material being ultralight. This is done by devising a 3D cubic auxetic unit cell that is inspired from a re-entrant two-dimensional auxetic unit cell [40]. The reported microlattice consists of a network of 3D isotoxal unit cells [shown in Fig. 1(a)]. Each unit cell comprises 30 solid cylindrical rods of the same diameter and intrinsic material. Among these, 24 inner rods make up three mutually perpendicular isotoxal square stars in the $x$-$y$, $y$-$z$, and $z$-$x$ planes, while six slightly smaller outer rods connect the unit cell to its adjacent neighbors. As illustrated in Fig. 1(b), the defining dimensions of this geometry are $p$, $d$, $a$, and $\theta$, where $p$ and $a$ refer to the periodicity and the distance between the vertices of the squares, respectively, while $d$ denotes the diameter of the rods and $\theta$ is the angle that the inner rods make with the vertical normal. The numerical results in Fig. 5 of Appendix A, illustrate the auxetic behavior of the sample as a function of $\theta$ and $d/p$. The intrinsic material properties that are employed for this simulation and for the ones that follow, are consistent with that of the base material that is later employed for the fabrication of the prototype (Young's modulus, $E = 512$ MPa; density, $\rho = 1.1$ g/cm$^3$; intrinsic Poisson's ratio, $\nu = 0.3$).

## III. ELASTIC WAVE DISPERSION

The elastic wave dispersion through the microlattice is then systematically studied by calculating its band structure and dynamic effective properties. Eigenfrequency simulations are first carried out on a single unit cell of the metamaterial with Floquet periodic boundary conditions. Here, the parameter $a$ is fixed to $0.8p$, $d$, at $0.06p$ and the value of $\theta$ is chosen to be 20°. The band structure for a sample of these dimensions is shown in Fig. 1(d) and indicates that two complete BGs of fractional bandwidths, 16.1% and 82.8%, are observed (regions shaded in gray) in the normalized frequencies ($f.p$) ranging from 22.9 to 26.9 and from 45.95 to 110.95, respectively. The occurrence of such low-frequency BGs can be attributed to local resonances that arise as a result of nodes 1 and 2 [shown in Fig. 1(b)] playing the role of two distinct masses and springs. This is in stark contrast to conventional 3D microlattices [19,41,42] and elastic metamaterials [7–15], where all the vertices of the lattice are identical and therefore contain only one type of homogeneous nodal structure as illustrated in Appendix B. In this case, however, the unit-cell topology reveals two distinct types of nodal structures as shown in Fig. 1(b). Here, node 1 is attached to five rods in total (four inner and one outer), while node 2 is attached only to two inner rods. This distinction allows for the existence of the two very different local resonance modes shown in Figs. 1($c_1$) and 1($c_2$) and in turn gives rise to the two distinct BGs in Fig. 1(d). The nodal structures

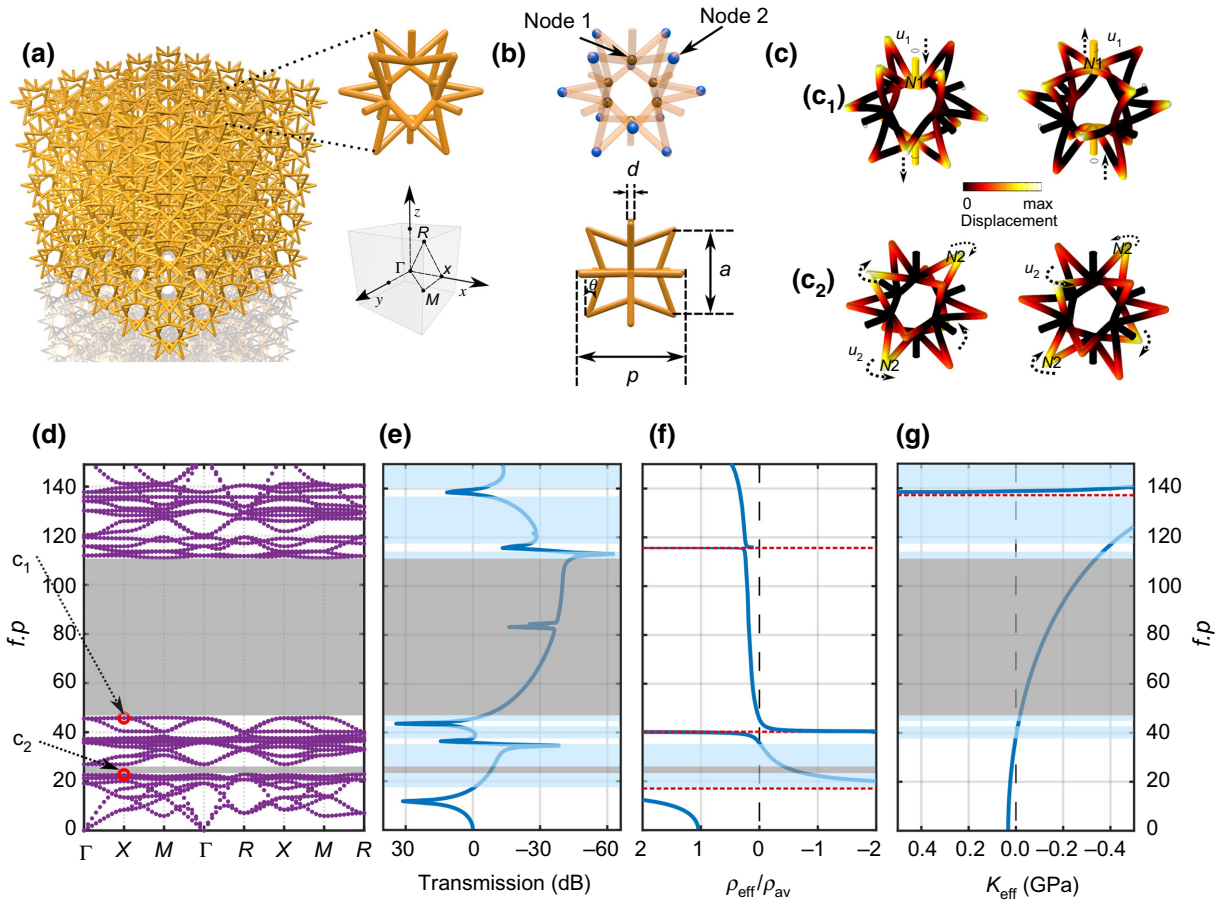


FIG. 1. (a) Ultralight microlattice-based elastic metamaterial composed of periodic auxetic building blocks (top right) and the directions of the irreducible Brillouin zone, for the simple cubic unit cell (bottom right). (b) (Top) Nodes 1 and 2 of the unit cell, denoted by the black and blue spheres, respectively. (Bottom) Dimensions of the unit cell: $p$ is the periodicity, and $a$ is the distance between the vertices of the isotoxal squares, $\theta$ is the angle between the outer edges of the isotoxal square stars and the vertical. (c) Snapshots of the resonance modes that give rise to band gaps. $u_1$ and $u_2$ denote the longitudinal and torsional displacement of the nodes 1 (N1) and 2 (N2), respectively. (d) Normalized band structure for the simple cubic auxetic unit cell along the different directions of the IBZ, for $\theta = 20^\circ$, $a = 0.8p$, and $d = 0.060p$. ($c_1$) and ($c_2$) are the modes at the $X$ point (red circles) on the lower edges of the BGs. (e) Longitudinal wave transmission in dB, for propagation in the $\Gamma$-$X$ direction. Frequency dependent (f) effective density, $\rho_{\text{eff}}$, and (g) effective bulk modulus, $\kappa_{\text{eff}}$. The dashed red lines in (f) and (g) indicate sudden jumps in $\rho_{\text{eff}}$ and $\kappa_{\text{eff}}$, from positive to negative values and vice versa. The regions in gray denote complete BGs, while those shaded blue indicate the BGs associated with longitudinal waves only.

comprise local mass-spring systems that can be analyzed via a lumped mechanical model (Appendix C), with their masses at nodes 1 and 2, i.e., $m_1$ and $m_2$, and the effective stiffnesses of the interconnecting springs, $K_1$ and $K_2$, obtained by calculating the reaction force and displacement under a global excitation [Figs. 7, 8, Eqs. (C1), (C5), (C13), and (C14)]. It is found that $K_1$ is over 2 orders of magnitude higher than $K_2$. For an example of the geometric parameters chosen here, $K_1$ has a stiffness of 150 kN/m, while $K_2$ is 500 N/m. Since the frequency of resonance is directly proportional to the square root of the stiffness, this would explain why (1) the BG associated with node 2 can occur at a very low frequency even with a small mass density (0.034 g/cm$^3$); (2) the BG associated with node 1 would occur at a higher frequency than that associated with node 2, due to its larger stiffness. Figures 1($c_2$) and 1($c_1$) show the mode behaviors of the unit cell at the lower edges of the first and second BGs, respectively. Figure 1($c_2$) indicates the resonance associated with $K_2$ since the outer rods that connect to node 1 remain stationary, while the inner rods that connect to node 2 are in torsional oscillation. Similarly, Fig. 1($c_1$) indicates the resonance associate with $K_1$ that occurs at a higher frequency and therefore corresponds to the case where the inner rods remain stationary while the outer rods experience a high degree of flexibility that allows them to vertically bounce on node 1. The wave behavior observed here is very similar to the motion offered by a trampoline as indicated by the dashed arrows in Fig. 1($c_1$). For a better visualization of the aforementioned modes, the reader is referred to the animation shown

in the Supplemental Material [53]. Since the geometry of the unit cell obeys cubic symmetry, the mode shape shown here is indicative of the displacement that would exist in the *x*-*y* and *y*-*z* planes. Such a distinctive wave behavior was previously known to exist only in the case of pillared plates [16,17], where the trampolinelike mode was shown to amplify the effect of the local resonance and therefore increase the width of its associated BG. A unique 3D trampoline behavior that amplified the effect of the local resonance is now seen in a lightweight 3D microlattice and enables the second BG of width 82.8%. This mode transcends the requirement for heavy masses or multiple materials employed in 3D elastic metamaterials to induce local resonance [7–15,38,43–45].

To further elucidate the origin behind the aforementioned BGs, frequency-domain simulations are then performed by applying a longitudinal excitation on one face of the unit cell and then extracting the dynamic effective properties at the $X$ point of the irreducible Brillouin zone (IBZ). Figure 1(e) shows the simulation result for the longitudinal-wave transmission through the $\Gamma$-$X$ direction of the metamaterial. This curve clearly illustrates very low transmission in the regions that correspond to the two complete BGs, marked by the shaded gray regions in Figs. 1(d) and 1(e). Additionally, in the case of Fig. 1(e), one can also observe very low transmission in the regions that are shaded blue, owing to the BGs that exist here for longitudinal waves only. The physical properties of the BGs in both the gray and blue regions can be further explained by calculating the frequency-dependent density [46], $\rho^{\text{eff}}$, and bulk modulus [47], $\kappa^{\text{eff}}$. This is done by evaluating the average resultant forces, displacements, stresses, and strains, along each of the unit cell's boundaries and then incorporating them in the formulation shown in Appendix D. It must be noted that a longitudinal excitation along the $\Gamma X$ direction is chosen here as an illustrative example to calculate the dynamic effective properties of the metamaterial. Since the associated BGs are in all directions and for all modes, one could employ this method, for shear elastic modes and for other directions of propagation as well.

Figure 1(f) shows the result for the dynamic effective density, normalized by the average density of the unit cell, $\rho_{\text{av}}$, and Fig. 1(g) shows the curve for dynamic effective bulk modulus as a function of the frequency. It is worthwhile to note that the effective density and moduli studied here, are frequency dependent and hence different from the static negative material properties that are conventionally studied in the case of auxetic materials. It can be observed that the narrow BGs at the lower frequencies are due to negative density and positive bulk modulus, while the wider ones at slightly higher frequencies come as a result of negative bulk modulus and positive density. This is true for the complete BGs (marked by the gray regions) as well as for the ones that exist only for longitudinal waves (marked by the blue regions). The wider BG that occurs between $f.p = 45.95$ and 110.95, corresponds to a region that efficiently couples a large negative effective modulus with a positive near-zero effective density. The wide-band performance enabled here is in stark contrast to the current state of the art in 3D elastic metamaterials [7–12,14,15,38,43–45], where masses are employed in the unit cells. Although prior studies did not shed light on the dynamic effective properties of the 3D metamaterials, the fact that they rely on heavy masses suggests that the associated BGs are purely based on negative density. The BG associated with the trampolinelike resonance reported here is thus a departure from the status quo and offers an advanced route for 3D vibration control. Additionally, the sudden peaks that lie between any two adjacent BGs in the transmission curve, occur as a result of the effective properties being either both positive or both negative. Such a double negative behavior in an ultralight metamaterial could also greatly aid applications like negative refraction [48] and superfocusing [49], that have only been realized for 2D elastic wave propagation to date.

## IV. BAND-GAP TAILORABILITY

Furthermore, the width and frequency ranges of the complete BGs can be conveniently tuned via the geometrical parameters of the unit cell. Altering the geometrical parameters allows for the judicious and simultaneous tailoring of the widths of both the negative density and modulus regions. For instance, Fig. 2(a) shows the evolution of two complete BGs as a function of $\theta$, for different values of $a$, while the value of $d$ is fixed at $0.06p$. It can be observed here, that decreasing the value of $a$ increases the frequencies at which these BGs occur. Further, this also lowers the frequency of the mode that exists between the two BGs, thereby increasing the width of the high-frequency BG, while reducing that of the lower one. Additionally, when the value of $a$ reaches $0.8p$, the increased length of the inner rods allows for the existence of a lower-frequency torsional mode that gives rise to the negative density-based BG that is seen here and is also noted previously in Fig. 1(d). Similarly, Fig. 2(b) shows the variation of the two complete BGs as a function of $\theta$, for different values of $d$ when the value of $a$ is fixed at $0.8p$. In this case, it can be noted that increasing the value of $d$ would increase the mass of all the struts in unison and not just that of the outer rods. This would hence increase the frequency ranges at which both the BGs occur coherently, without much change to the width of the individual BGs. At much higher values of $d/p$, however, the negative density-based narrowband BG is replaced by multiple BGs of similar width. In addition to the geometrical parameters, the BGs can also be tailored via the properties of the intrinsic material that is employed for its fabrication. As

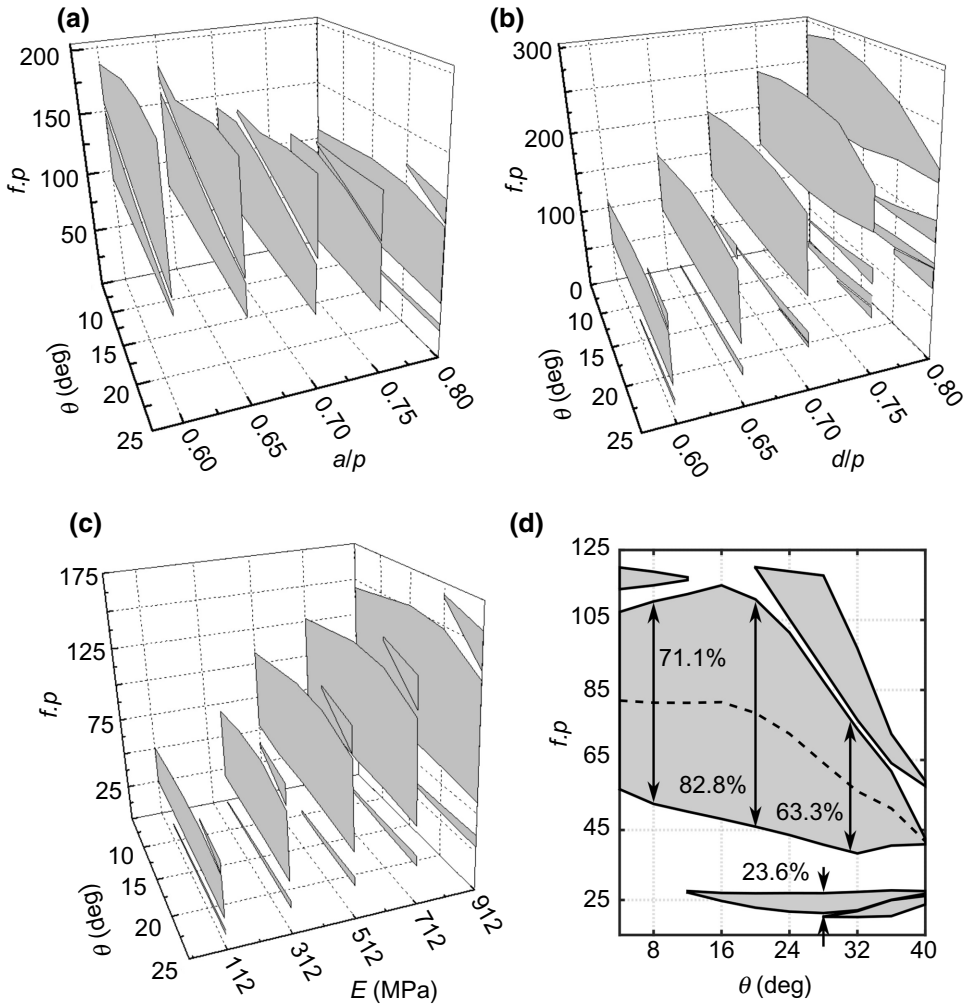


FIG. 2. Accessing band gaps that occur at other frequency ranges and/or with other bandwidths. (a) Evolution of the gaps as a function of the geometrical parameters, $a/p$ and $\theta$, when the value of $d$ is fixed at $0.06p$, (b) gaps as a function of $d/p$ and $\theta$, when the value of $a$ is fixed at $0.8p$, (c) the gaps evolve as a function of Young's modulus, $E$, and $\theta$, when $d$ and $a$ are fixed at $0.06p$ and $0.8p$, respectively ; (d) the evolution of the BGs (shaded gray regions), as a function $\theta$, for the unit cell where $d = 0.8p$, $a = 0.06p$, and $E = 512$ MPa, where the dashed black line indicates the central frequencies of the widest BG.

can be seen in Fig. 2(c), the frequency range of the BG can be considerably increased (decreased) by simply utilizing an intrinsic material that has a higher (lower) Young's modulus.

From Figs. 2(a) and 2(b), it can be seen that the BG associated with the trampoline mode appears widest when $a$ and $d$ are $0.8p$ and $0.06p$, respectively. These parameters are therefore fixed in order to further investigate the influence that the relative orientation, $\theta$, has on the BG behavior. As seen previously in Figs. 2(a)–2(c), multiple BGs can be opened and closed in this case as well, by simply tuning the value of $\theta$ alone. It must be noted here that the value of $\theta$ in this study is considered to lie only between 5° and 40°, so as to ensure that the vertices of the isotoxal stars do not overlap. Figure 2(d) shows the evolution of the complete BGs (shaded gray regions) as a function of $\theta$ and the dashed black line denotes the center frequency of the second BG that corresponds to the trampoline mode. It is evident here that the BG of interest would be at its widest and lowest, when $\theta = 20°$. A structure with these optimal dimensions is hence chosen as the candidate for the previous section and for the experimental study that follows.

Figure 3 compares the wave-attenuation performance of the present metamaterial with the previously reported 3D elastic metamaterials (mass densities and normalized frequencies, $f.p$) and the measured BGs associated with each study are, respectively, color coded. This chart indicates that our microlattice-based design (denoted by the bar in gray) can achieve wide BGs at low normalized frequencies and simultaneously possess the lowest effective density at a fraction of the density of previous metamaterials.

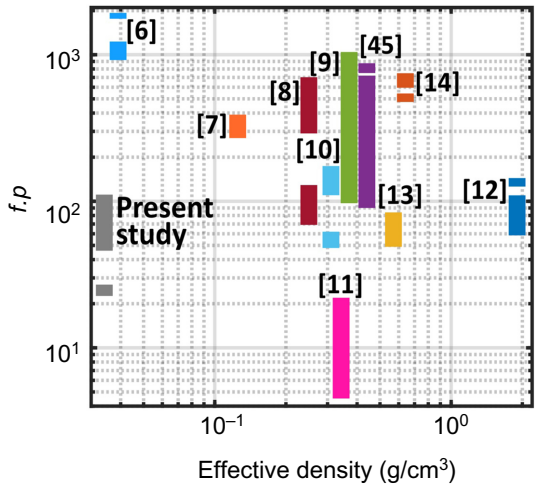


FIG. 3. Illustration of the ultralow effective density that is achieved in the study alongside the wave-attenuation performance at small values of normalized frequency ($f.p$), in comparison with the performance of relevant prior works. Each of the references is individually color coded and the height of the bars denote the regions of $f.p$ where their band gaps lie.

## V. EXPERIMENTAL REALIZATION

The fabrication of our intricate isotoxal-based elastic metamaterial is made possible by a high-resolution fabrication technique that is discussed in detail in Appendix E. Figure 9(b) shows photographs of the as-fabricated samples along three different orientations. These are the (1,0,0), (1,1,0), and (1,1,1) and are chosen to be consistent with the Γ-$X$, Γ-$M$, and Γ-$R$ directions of the IBZ shown in Fig. 1(a). Although the three samples have the same basic dimensions for $d$, $\theta$, and $a$, the periodicities of the metamaterial along the Γ-$X$, Γ-$M$, and Γ-$R$ directions are $p$, $\sqrt{2}p$, and $\sqrt{3}p$, respectively. Here, $p = 2$ cm, and the widths of the resultant samples are 6, 5.65, and 6.9 cm, and comprised of 3, 2, and 2 units, respectively. In addition to the lattice-based microstructure, the fabricated samples also had plates with a thickness of 3 mm on either side, for the convenience of the experimental characterization.

The transmission measurement through the sample is carried out by placing the Γ-$X$, Γ-$M$, and Γ-$R$ samples on a measurement platform as shown in Figs. 4(a)–4(c), respectively. The bottom plate of the sample is connected to a B&K 4809 mechanical shaker that facilitates the longitudinal excitations that serve as the input wave. The top plate, on the other hand, is connected to a PCB Piezotronics 352C33 accelerometer (100 mV/g) that measures the wave that transmits through the sample and reaches the other side. A schematic of the entire experimental setup is shown in Fig. 4(d), where the accelerometer is connected to an ICP Signal Conditioner (PCV 482C05), that transmits the acquired data to an SRS860 high-frequency lock-in amplifier. The lock-in amplifier is controlled by a custom LabView program, such that its internal oscillator is amplified by a B&K 2718 amplifier and in turn used to drive the mechanical shaker. The internal reference frequency of the SRS860 is programmed to cycle from 500 Hz to 10 kHz in ten steps, the data is sampled with a 10-ms time constant, and an 18-dB low-pass filter is applied to enable a high signal-to-noise ratio.

Figure 4(f) shows the complete band structure for the fabricated samples, where $p = 2$ cm and Fig. 4(e) denotes the results from numerical simulations that mimicks the experimental platform. In Fig. 4(e), the normalized displacement field for the Γ-$X$, Γ-$M$, and Γ-$R$ samples are shown for the case where the excitation is applied to the bottom plate (as indicated by the black arrows) and has a frequency that lies within the region of the BG. As can be seen here, when a wave of 4 kHz tries to propagate through the lattice, the trampolinelike behavior facilitates an extremely high wave attenuation by completely reflecting the incident energy. The wave, therefore, does not propagate through more than half a unit cell and enables high wave attenuation through a sample that has a very small number of unit cells (the animation of wave propagation through the lattice clearly illustrates this and can be found in the Supplemental Material [53]).

Figure 4(h) shows the experimentally obtained frequency-dependent transmission curves for the Γ-$X$, Γ-$M$, and Γ-$R$ samples. These are denoted here by the blue, orange, and red lines, respectively. All three curves undergo a sharp decay in transmission at the frequencies between 1.95 and 4.7 kHz and confirms the existence of a BG of width 82.7%, in this frequency range. This is in reasonable agreement with the trampoline-resonance-based BG of width 82.8%, that we expect to see between 2.3 and 5.55 kHz, from the numerical results. The shift of this BG to a slightly lower frequency range in the experimental results can be attributed to minor deviations in the stiffness of the intrinsic material. Furthermore, another cause for this shift could be the deviation in the geometrical parameter, $\theta$, that possibly arises due to the weight of the accelerometer that is placed on the top plate of the sample. One could envision that the weight associated with the accelerometer would increase the value of $\theta$ in the metamaterial unit cell [see Fig. 1(b)]. Judging from the plot in Fig. 2(d), increasing the value of $\theta$ would decrease the frequency of the second BG, and this is consistent with what is observed in the experiment. Further, the plot in Fig. 2(d) indicates that the increase in $\theta$ would open a third BG at higher frequencies. This therefore can also explain the dip that is seen at frequencies around 6 kHz, for the measured results but not the band structure in Fig. 4(f). To confirm the cause for this deviation, Fig. 4(g) shows the numerically calculated frequency-dependent transmission through the three samples with corrected values for Young's modulus, $E$, and angle, $\theta$ (i.e., $E = 415$ MPa instead of 512 MPa, and $\theta = 21^\circ$ instead of

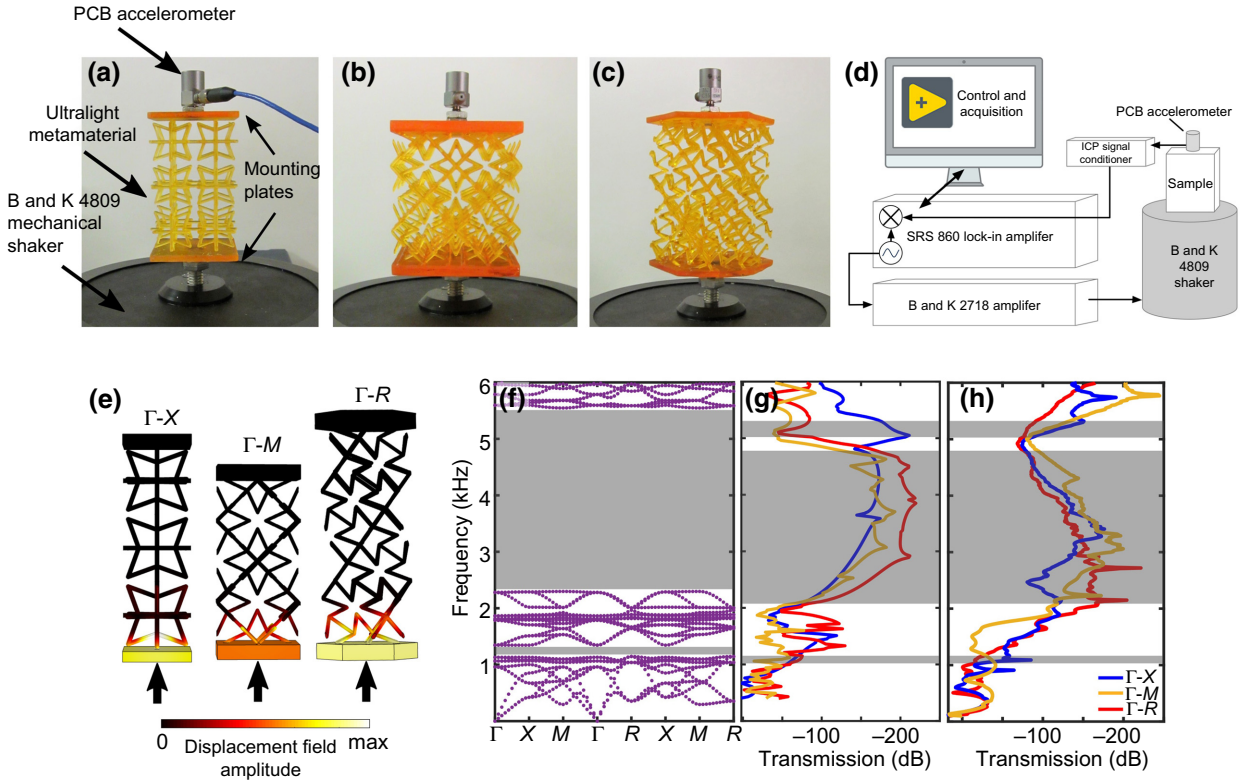


FIG. 4. Photograph of the measurement platform with the (a) Γ-$X$, (b) Γ-$M$, and (c) Γ-$R$ samples mounted, (d) schematic of the experimental measurement setup, (e) numerical results of the normalized displacement field for the Γ-$X$, Γ-$M$, and Γ-$R$ samples, for a frequency of excitation of 4 kHz, (f) band structure (in kHz), for the unit cell, where $\theta = 20^\circ$, $d = 0.06p$, and $a = 0.8p$, and the material properties are $E = 512$ MPa, $\nu = 0.3$, and $\rho = 1.1$ g/cm$^3$. (g) Results from frequency-domain transmission simulations through the three samples under consideration with $\theta = 21^\circ$, corrected material properties (shown in Fig. 10 in Appendix F) and an isotropic loss factor of 0.01. (h) Experimentally measured elastic wave transmission (dB) through the Γ-$X$, Γ-$M$, and Γ-$R$ samples—denoted by the blue, orange, and red curves, respectively. The shaded gray regions in (f)–(h), indicate the BGs.

20°) and demonstrate a closer agreement with the experimentally measured results. The material properties that are employed for this calculation and the relevant band structure can be found in Appendix F.

In both Figs. 4(g) and 4(h), besides the frequencies associated with the complete BGs, low transmission is also observed in the regions where there are BGs for longitudinal waves only. This is due to the fact that the input excitation here is purely longitudinal, as is the case in the experimental setup. The low-frequency BG of width 16.1%, that exists between 1.13 and 1.35 kHz, on the other hand, is quite narrowband and is hence challenging to observe in the experiments. To add to this, the frequency region associated with this narrowband BG (1–1.8 kHz) also possesses BGs for longitudinal waves. This is clearly observed in the numerical results in Fig. 4(g) and therefore makes it difficult to differentiate the different narrowband regions of low transmission in the experimental curves as well. However, a considerable dip can be seen in the case of the Γ-$M$ and Γ-$R$ curves, in the regions between 900 Hz and 1.05 kHz, which reasonably correspond to the negative density-based BG that is expected for this metamaterial. From both Figs. 4(g) and 4(h), one can also observe that the decay measured in the BG regions is highest in the case of the Γ-$R$ sample and lowest in the case of the Γ-$M$ sample. This is due to the proportionally different sample lengths in the three cases, with Γ-$R$ being the longest and Γ-$X$ being the smallest.

## VI. CONCLUSION

To summarize, we report an ultralight microlattice-based metamaterial that possesses 3D trampolinelike resonant modes and therefore achieves wide-band omnidirectional elastic wave attenuation. A lumped mechanical model is developed to analyze the system theoretically and its dynamic properties are numerically examined to unveil the effective density and modulus that are associated with the 3D trampoline-induced BG. Furthermore, it is demonstrated that the widths and frequency ranges of the BGs associated with this metamaterial can be conveniently tuned via the geometrical parameters of the microlattice.

The metamaterial with desirable characteristics is then fabricated by our unique manufacturing capability and experimentally characterized to corroborate the results in our numerical simulations. It is observed here that the trampolinelike mode enables complete wave reflection in the BG region, with a very small number of unit cells. Such a high wave attenuation, accompanied by an ease of tailorability, can be leveraged to further increase the width of the BG (an example that numerically illustrates this in one wave propagation direction can be found in Appendix G). In addition to its elastodynamic functionality, the proposed metamaterial also possesses a second-order functionality of exhibiting auxeticity or a static negative Poisson ratio. This would greatly aid applications that demand a marriage of these unrelated yet highly advantageous functionalities. Both the auxetic and elastodynamic performance could also be further enhanced via the use of multiple materials in the microlattice [21,50]. In contrast to the existing strategies for vibration attenuation, which are heavy and/or relatively impervious, the material introduced here has a 97% porosity and could also allow the coexistence of other functionalities like thermal insulation and airborne sound absorption, which were previously unattainable. Lastly, the tailorability of this design could also be leveraged in the future for adaptive and reconfigurable elastic wave control.

## ACKNOWLEDGMENTS

Y.J. acknowledges the startup support from Penn State University. Z.X., H.C., D.Y. and X.Z. thank the Air Force Office of Scientific Research (FA9550-18-1-0299), Office of Naval Research (N00014-18-1-2553 and N00014-19-1-2723), DARPA D20AP00001-02, and the National Science Foundation (2001677) for their financial support. C.N., A.I., and C.R. are supported by the Office of Naval Research.

N.J.G., M.O., Z.X., and D.Y. contributed equally to this work. N.J.G. and M.O. performed the design and numerical simulations. Z.X. and H.C. fabricated the samples. D.Y. built the theoretical model and helped with mechanical interpretations. C.J.N., A.I., and C.A.R. carried out the transmission experiments. N.J.G., M.O., X.Z., and Y.J. wrote the paper with contributions from all the authors. Y.J. and X.Z. supervised the project.

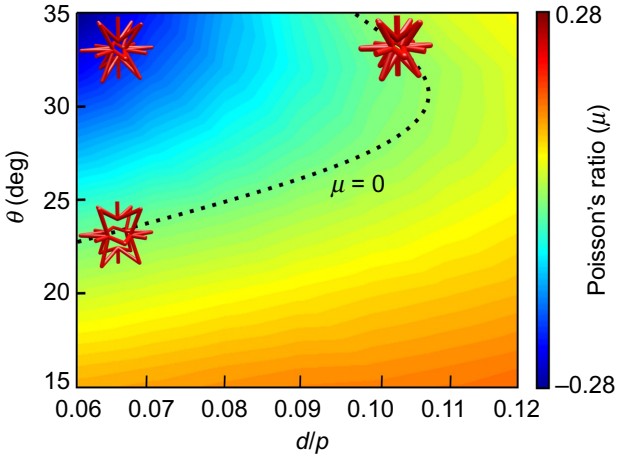


FIG. 5. Poisson's ratio, $\mu$, for different values of $\theta$ and $d/p$, when $E = 512$ MPa, $a = 0.8p$, $\nu = 0.3$, $\rho = 1.1$ g/cm$^3$. Insets show the geometry of the unit cell for the larger negative value of $\mu$ and for when $\mu = 0$.

## APPENDIX A: STATIC NEGATIVE POISSON'S RATIO OF THE 3D ISOTOXAL-BASED ELASTIC METAMATERIAL

To verify the auxeticity of the proposed metamaterial, static numerical simulations are carried out using the solid mechanics module on COMSOL Multiphysics 5.3(a). A known longitudinal displacement is prescribed on one face of a finite sample made up of $3 \times 3 \times 3$-unit cells and the resultant lateral displacement is extracted by the method described in Ref. [51], to estimate Poisson's ratio of the bulk material. The plot in Fig. 5 indicates that the proposed 3D metamaterial exhibits auxeticity when the chosen geometrical parameters lie in the region above the dashed curve, which corresponds to $\mu = 0$. Poisson's ratio can be further lowered by decreasing (increasing) the value of $d/p$ ($\theta$) and can reach a minimum of $\mu = -0.28$ for $\theta = 34^\circ$ and $d = 0.06p$.

## APPENDIX B: DESCRIPTION OF THE TWO NODES

Most microlattice-based metamaterials comprise vertices that are identical and can be described only by one

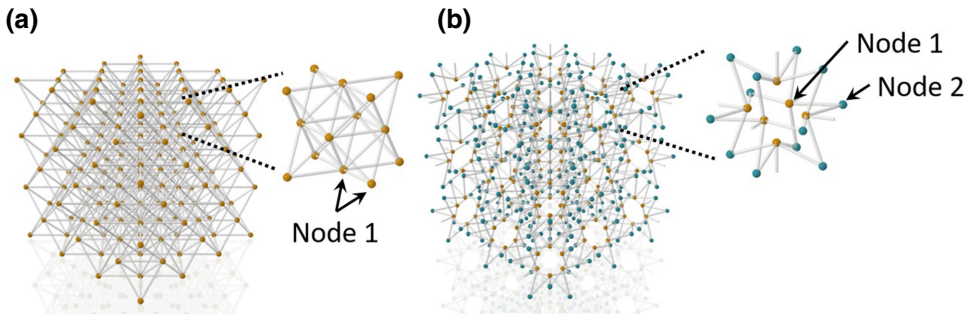


FIG. 6. (a) Identical nodes in a conventional octet-truss lattice [19,42]. (b) The two different nodes of the isotoxal auxetic unit cell that is proposed here.

of kind of node, as shown in an illustrative example in Fig. 6(a). The prominent octet-truss lattice [19,42] in Fig. 6(a) would therefore possess only one uniform set of natural frequencies. In the metamaterial proposed in this work however, there are two types of nodes as shown in Fig. 6(b). Node 1 is connected to a total of five struts (four inner and one outer), while the node 2 is connected only to two inner struts.

## APPENDIX C: THEORETICAL MODEL TO EVALUATE MASS AND STIFFNESS

The unit cell of the proposed metamaterial [shown in Fig. 7(a)] can be described as a combination of two different masses and springs, as illustrated in Fig. 7(b). Here mass 2 ($m_2$) is connected to mass 1 ($m_1$) through a spring $K_2$, and $m_1$ is in turn connected to the neighboring unit via a spring $K_1$. Such a system would therefore possess resonances that arise as a result of $m_1$-$K_1$ as well as $m_2$-$K_2$ and would thus give rise to the two different BGs that are seen in Fig. 1(d). Since node 1 is connected to five struts, the total mass of $m_1$, can obtained by first expressing the effective length of the strut in terms of the angle, $\theta$, shown in Fig. 7(c). the resultant expression for $m_2$ would therefore be

$$m_1 = \left(\frac{a}{2\cos\theta} + \frac{p + a(\tan\theta - 1)}{8}\right)\rho\pi d^2. \tag{C1}$$

The effective stiffness of the spring, $K_1$, can then be evaluated by calculating the total reaction force, $F_{t1}$, at node 1 that would impose a unit displacement, $\delta_1$. $F_{t1}$ can in turn be expressed as the sum of the reaction forces that occur in the vertical strut and the four inclined struts that are denoted below by $F_{v1}$ and $F_{i1}$, respectively. These can be calculated via the expressions for the bending deflection of a simply supported beam and would give

$$F_{v1} = \frac{E\pi d^2\delta_1}{2p + 2a(\tan\theta - 1)}, \tag{C2}$$

$$F_{i1} = \frac{E\pi d^2}{a}\left(\frac{3d^2\cos^5\theta}{8a^2} + \frac{\sin^2\theta\cos\theta}{2}\right). \tag{C3}$$

The effective stiffness of the spring, $K_1$, can hence be obtained as

$$K_1 = \frac{F_{t1}}{\delta_1} = \frac{4F_{i1} + F_{v1}}{\delta_1}, \tag{C4}$$

which results in the following expression for the local effective stiffness of node 1:

$$K_1 = \left[\frac{3d^2\cos^5\theta}{2a^3} + \frac{2\sin^2\theta\cos\theta}{a} + \frac{1}{2p + 2a(\tan\theta - 1)}\right]E\pi d^2. \tag{C5}$$

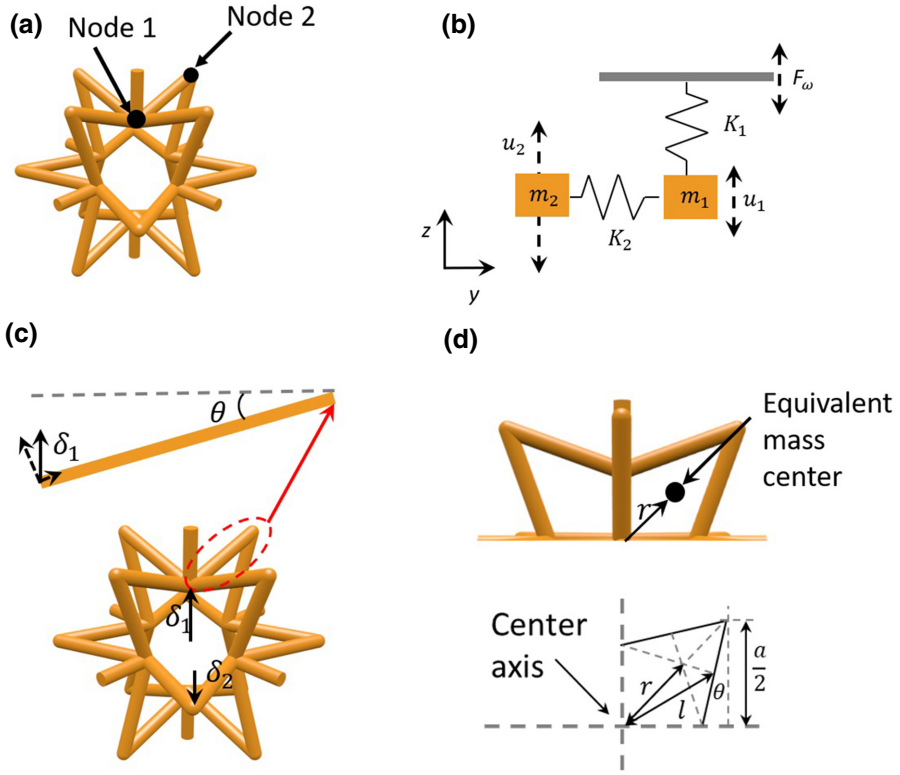


FIG. 7. (a) Unit cell of the proposal 3D elastic metamaterial with the two nodes described in Appendix B, (b) shows its equivalent spring-mass system. $F_\omega$ is the external excitation, while $u_1$ and $u_2$ denote the displacements of the individual masses. (c) The bottom shows the isotoxal auxetic unit cell that experiences the displacements, $\delta_1$ and $\delta_2$ at nodes 1 and 2, respectively. The top shows node 1 attached to an inclined strut, with an angle, $\theta$. (d) The top shows the equivalent mass center for node 2 that is offset from the center axis and the bottom indicates the parameters, *r,* and *l*, in this context.

Node 2, on the other hand, is modeled as one that possess a torsional spring, since the equivalent mass at node 2, is offset from the central axis by a distance, $r$, as denoted in Fig. 7(d). As per the parallel axis theorem, the total moment of inertia at this node, $J_2$, can be calculated as

$$J_2 = 2J + 2Ml^2, \tag{C6}$$

where $J$ refers the moment of inertia of each strut to its center and $M$ denotes the mass of the strut, both of which can be calculated as

$$J = \frac{1}{12}ML^2 = \frac{1}{12}\rho\pi\left(\frac{d}{2}\right)^2\left(\frac{a}{2\ \cos\ \theta}\right)^3, \tag{C7}$$

$$M = \frac{a}{8\ \cos\ \theta}\rho\pi d^2, \tag{C8}$$

where $l$ is the distance from the strut center to the center axis. The torsional stiffness, $\kappa_2$, of the spring at node 2 can then be calculated as done previously, by using the total reaction force, $F_{t2}$, for the case of a unit displacement, $\delta_2$, and can be expressed as

$$\kappa_2 = \frac{F_{t2}r^2}{\delta_2}. \tag{C9}$$

$F_{t2}$ in this case can be calculated through the expression,

$$F_{t2} = \frac{48EI\delta_2\ \cos^3\theta}{a^3}. \tag{C10}$$

The distance $r$ can be calculated by

$$r = \frac{a}{2}\left[\frac{\cos(45^\circ - \theta)}{3\ \cos\ \theta} + \frac{\sqrt{2}}{2}(1 - \tan\ \theta)\right]. \tag{C11}$$

The effective stiffness, $\kappa_2$, of the torsional spring would therefore be equivalent to

$$\kappa_2 = E\pi d^2\frac{3d^2\ \cos^3\theta}{a}\left[\frac{\cos(45^\circ - \theta)}{3\ \cos\ \theta} + \frac{\sqrt{2}}{2}(1 - \tan\ \theta)\right]^2. \tag{C12}$$

Lastly, the mass and stiffness of node 2 can be calculated by writing $m_2 = J_2/r^2$ and $K_2 = \kappa_2/r^2$ and would subsequently yield the following expressions:

$$m_2 = \frac{\rho\pi d^2}{16}\left[\frac{a}{3\ \cos^3\theta} + \frac{a(\tan^2\theta - 4\ \tan\ \theta + 5)}{\cos\ \theta}\right] \times \left[\frac{\cos(45^\circ - \theta)}{3\ \cos\ \theta} + \frac{\sqrt{2}}{2}(1 - \tan\ \theta)\right]^{-2}, \tag{C13}$$

$$K_2 = E\pi d^2\frac{3d^2\cos^3\theta}{4a^3}. \tag{C14}$$

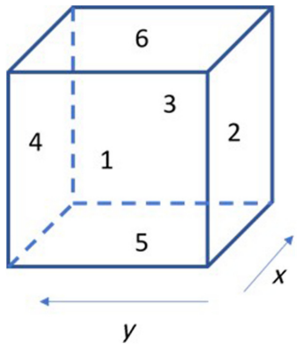


FIG. 8. Labeled boundaries 1–6 of the cubic unit cell.

## APPENDIX D: EVALUATION OF THE DYNAMIC EFFECTIVE PROPERTIES

The theoretical characterization of the effective parameters is achieved by calculating the average forces, displacement, stress and strain of the unit cell along boundaries 1–6, shown in Fig. 8. The calculations are performed at the $X$ point of the irreducible Brillouin zone. $F_x^{\text{eff}}$ and $U_x^{\text{eff}}$ can be obtained by averaging the stress along the boundaries of the unit cell,

$$F_x^{\text{eff}} = -\int_1 T_{xx}ds + \int_3 T_{xx}ds - \int_2 T_{xy}ds + \int_4 T_{xy}ds - \int_5 T_{xz}ds + \int_6 T_{xz}ds, \tag{D1}$$

$$U_x^{\text{eff}} = \frac{1}{2p^2}\left(\int_1 u_x ds + \int_3 u_x ds\right). \tag{D2}$$

Likewise, the components of the effective stress and strain tensors, $T_{ij}^{\text{eff}}$ and $S_{ij}^{\text{eff}}$, the effective elastic constants, $C_{ij}^{\text{eff}}$, can be calculated as

$$T_{xx}^{\text{eff}} = \frac{1}{2p^2}\left(\int_1 T_{xx}ds + \int_3 T_{xx}ds\right),$$

$$T_{yy}^{\text{eff}} = \frac{1}{2p^2}\left(\int_2 T_{yy}ds + \int_4 T_{yy}ds\right),$$

$$T_{zz}^{\text{eff}} = \frac{1}{2p^2}\left(\int_5 T_{zz}ds + \int_6 T_{zz}ds\right),$$

$$T_{xy}^{\text{eff}} = \frac{1}{2p^2}\left(\int_2 T_{xy}ds + \int_4 T_{xy}ds\right),$$

$$S_{xx}^{\text{eff}} = \frac{1}{p^3}\left(\int_3 u_x ds - \int_1 u_x ds\right),$$

$$S_{yy}^{\text{eff}} = \frac{1}{p^3}\left(\int_4 u_y ds - \int_2 u_y ds\right),$$

$$S_{zz}^{\text{eff}} = \frac{1}{p^3}\left(\int_6 u_y ds - \int_5 u_y ds\right),$$

$$S_{xy}^{\text{eff}} = \frac{1}{2p^3}\left(\int_4 u_x ds - \int_2 u_x ds\right) + \frac{1}{2p^3}\left(\int_3 u_y ds - \int_1 u_y ds\right). \tag{D3}$$

The stress-strain matrix for a three-dimensional cubic unit cell can be written as [47]

$$\begin{pmatrix} T_{xx}^{\text{eff}} \\ T_{yy}^{\text{eff}} \\ T_{zz}^{\text{eff}} \\ T_{yz}^{\text{eff}} \\ T_{xz}^{\text{eff}} \\ T_{xy}^{\text{eff}} \end{pmatrix} = \begin{pmatrix} C_{11}^{\text{eff}} & C_{12}^{\text{eff}} & C_{12}^{\text{eff}} & 0 & 0 & 0 \\ C_{11}^{\text{eff}} & C_{11}^{\text{eff}} & C_{12}^{\text{eff}} & 0 & 0 & 0 \\ C_{12}^{\text{eff}} & C_{12}^{\text{eff}} & C_{11}^{\text{eff}} & 0 & 0 & 0 \\ 0 & 0 & 0 & C_{44}^{\text{eff}} & 0 & 0 \\ 0 & 0 & 0 & 0 & C_{44}^{\text{eff}} & 0 \\ 0 & 0 & 0 & 0 & 0 & C_{44}^{\text{eff}} \end{pmatrix} \begin{pmatrix} S_{xx}^{\text{eff}} \\ S_{yy}^{\text{eff}} \\ S_{zz}^{\text{eff}} \\ 2S_{yz}^{\text{eff}} \\ 2S_{xz}^{\text{eff}} \\ 2S_{xy}^{\text{eff}} \end{pmatrix}, \tag{D4}$$

where $T_{ij}^{\text{eff}}$ and $S_{ij}^{\text{eff}}$ are the components of the effective stress and strain tensors, respectively, with $i$ and $j$ representing the different directions of propagation, i.e., $i \in \{x, y, z\}$. These stress and strain values are calculated for each frequency as per the method described above and employed to compute the effective elastic constants, $C_{ij}^{\text{eff}}$. The effective bulk modulus is then obtained using the expression,

$$\kappa_{\text{eff}} = \frac{C_{11}^{\text{eff}} + C_{12}^{\text{eff}}}{2}. \tag{D5}$$

Likewise, the effective density, $\rho_{\text{eff}}$, is calculated through Newton's second law, by the following expression [46]:

$$\begin{pmatrix} F_x^{\text{eff}} \\ F_y^{\text{eff}} \\ F_z^{\text{eff}} \end{pmatrix} = \begin{pmatrix} \rho_{xx}^{\text{eff}} & \rho_{xy}^{\text{eff}} & \rho_{xz}^{\text{eff}} \\ \rho_{yx}^{\text{eff}} & \rho_{yy}^{\text{eff}} & \rho_{yz}^{\text{eff}} \\ \rho_{zx}^{\text{eff}} & \rho_{zy}^{\text{eff}} & \rho_{zz}^{\text{eff}} \end{pmatrix} \begin{pmatrix} U_x^{\text{eff}} \\ U_y^{\text{eff}} \\ U_z^{\text{eff}} \end{pmatrix}, \tag{D6}$$

where $F_i^{\text{eff}}$ and $U_i^{\text{eff}}$, refer to the effective forces exerted and the resultant displacements along the $i$th direction of the unit cell and can be calculated through Eqs. (D1) and (D2). Since the excitation here is purely longitudinal, this study is focused on extracting the effective properties only for the longitudinal mode thereby focusing only on the diagonal terms of the matrix in Eq. (D6). Additionally, due to the cubic symmetry, the diagonal terms of the effective density matrix would be equal, i.e., $\rho_{xx}^{\text{eff}} = \rho_{yy}^{\text{eff}} = \rho_{zz}^{\text{eff}}$, and would hence further reduce Eq. (D6) to

$$\rho_{\text{eff}} = -\frac{F^{\text{eff}}}{\omega^2 p^3 U^{\text{eff}}}. \tag{D7}$$

## APPENDIX E: SAMPLE FABRICATION

The fabrication of our intricate isotoxal-based elastic metamaterial is made possible by a high-resolution, large-area projection microstereolithography (LAP$\mu$SL) platform that utilizes a layer-by-layer digital light manufacturing technique, as shown in Fig. 9(a). LAP$\mu$SL [19,42,52] is capable of fabricating complex structures with feature sizes ranging from microns to a few centimeters. Firstly, in order to enable the printability of the lattice, supports (that

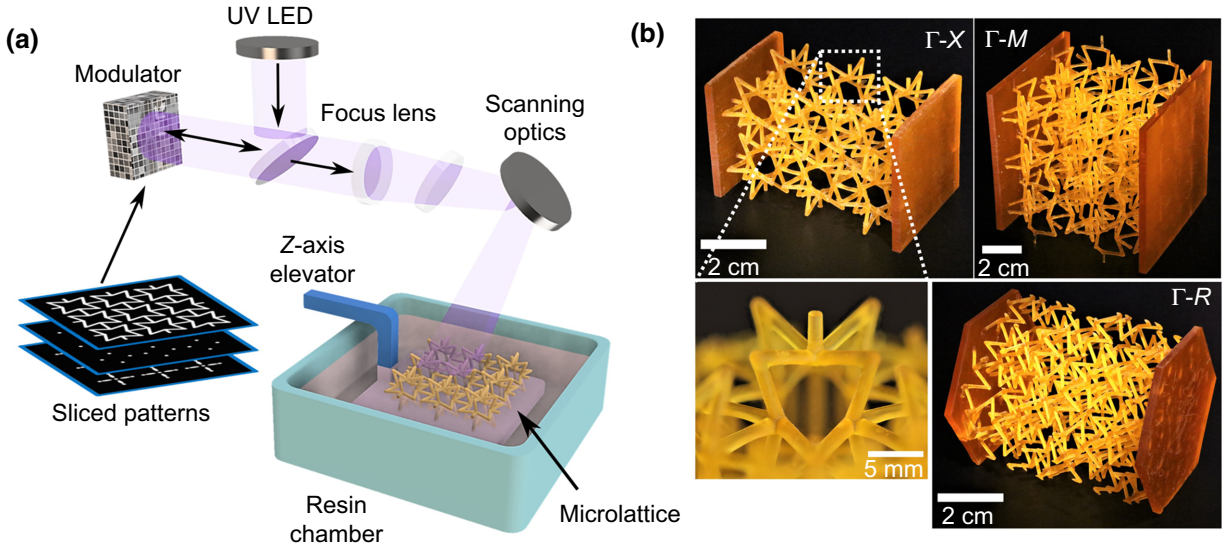


FIG. 9. (a) Schematic illustration of the fabrication technique. (b) Photographs of the ultralight isotoxal star-based metamaterial samples, fabricated in the Γ-$X$ (top left), Γ-$M$ (top right), and Γ-$R$ (bottom right) directions, with the same unit-cell dimensions and with period, $p = 2$ cm. Bottom left shows a close-up optical image of the Γ-$X$ sample, featuring the overhanging structure in the present metamaterial.

can later be removed or dissolved) are added at the overhanging positions. The three-dimensional computer aided design (CAD) model of the sample is then sliced into a group of two-dimensional images, which are subsequently transmitted to a digital micromirror device (DMD) chip. The UV light from the diode array is patterned by the modulator and then transmitted through a lens system to reduce the pattern size and to increase the resolution. The patterned UV light is then projected onto the surface of a UV-curable resin to form the shape of the 2D slice on a printing substrate. After the curing of the first layer, the printing substrate is lowered for the recoating of the liquid resin and the process is repeated until the formation of the whole 3D microlattice. The scalability of the fabrication system is expanded by coordinating the projection setup with an optical scanning system, which allows the UV pattern to be exposed to different areas within a single layer. After printing, the samples are cleaned with ethanol, the internal supports are removed, and then postcured under UV light. The material employed here is composed of a polymer (1,6-Hexanediol diacrylate), photoinitiator [phenylbis(2,4,6-trimethylbenzoyl)phosphine oxide], and photoabsorber (Sudan 1). The material properties of this resin are consistent with the values incorporated in the numerical simulation (Young's modulus, $E = 512$ MPa; density, $\rho = 1.1$ g/cm$^3$; intrinsic Poisson's ratio, $\nu = 0.3$).

## APPENDIX F: CORRECTED BAND STRUCTURE FOR THE EXPERIMENTALLY MEASURED SAMPLES (Fig. 10)

The frequency domain transmission results shown in Fig. 4(g), was obtained through corrected values for the material properties. Figure 10(a) shows the bandstructure for the unit cell with the corrected values and illustrates good agreement with the experimentally measured results shown in Fig. 10(b) [same as the one in Fig. 4(h)].

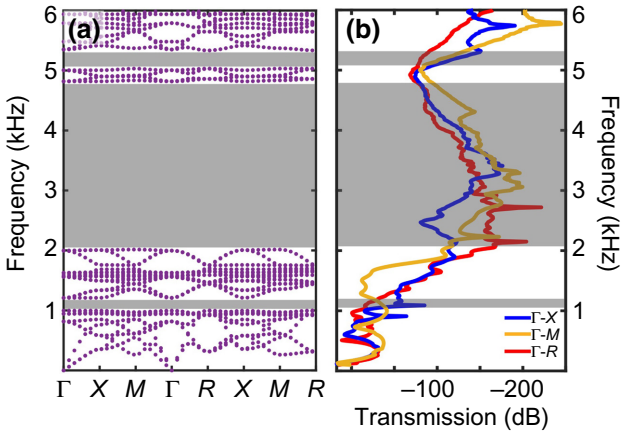


FIG. 10. (a) Complete band structure for a sample of dimensions, $p = 2$ cm, $a = 1.6$ cm, $d = 1.2$ mm, $\theta = 21°$, and material properties, $E = 415$ MPa, $\nu = 0.3$, and $\rho = 1.1$ g/cm$^3$. (b) Measurement results for frequency-dependent transmission, for samples along the Γ-$X$, Γ-$M$, and Γ-$R$ directions, also shown in Fig. 4(h).

## APPENDIX G: HYBRID METAMATERIAL SAMPLE WITH AN EXTREMELY WIDE BAND GAP

The hybrid sample can be made possible by combining three pairs of unit cells with different but overlapping band gaps. Here, the three-unit cells chosen have the same $\theta$ value but different $d$ values. The values of $d$ are chosen from the band-gap analysis, which is shown in Fig. 2(a) of the main text. At first, the transmission performance for each of the cases are examined when only two-unit cells are considered. Figure 11(a) here, shows the transmission results for $d = 0.06p$, $0.08p$, and $0.10p$, which are denoted by the red, blue, and green curves, respectively. High attenuation of the wave is clearly seen in the desired frequency ranges for each of the cases: $f.p$ from 46 to 111 for $d = 0.06p$; from 68.2 to 150.8, for $d = 0.08p$ and

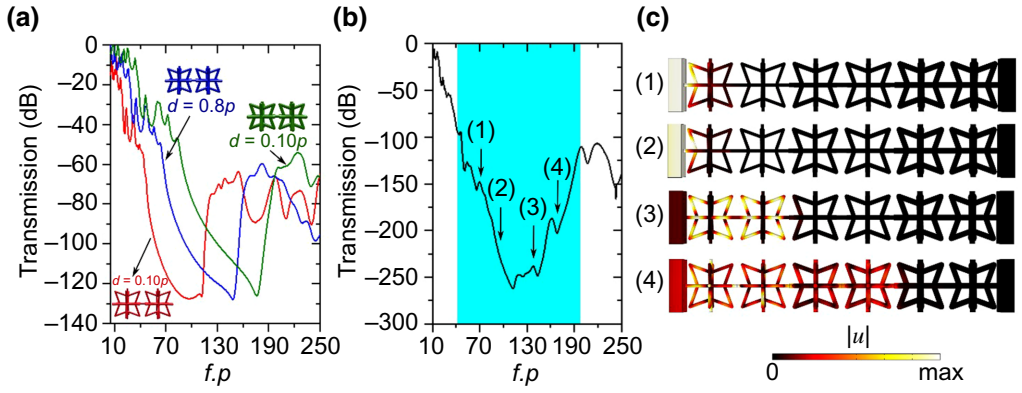


FIG. 11. (a) Transmission (dB), through two-unit cells for the cases of $d = 0.06p$, $d = 0.08p$, and $d = 0.10p$. (b) Elastic wave transmission in the Γ-$X$ directions, through the hybrid sample made up of the three sets of unit cells. (c) Normalized displacement field amplitude through the sample for the four different frequencies that are indicated in the transmission spectrum in (b).

from 90 to 184, for $d = 0.10p$. The three units are then combined and the wave transmission through this hybrid design can be seen in Fig. 11(b). An overall attenuation can be seen in the frequency ranges of the three individual band gaps seen in Fig. 11(a). Figure 11(c) shows the normalized displacement field amplitude for the hybrid microlattice along its $\Gamma$-$X$ direction, at the frequencies indicated by (1) inside the first band gap but outside the second, (2) inside the common the regions of the three band gaps, (3) inside the second and the third band gap, and (4) inside the third band gap, but outside the others. The waves of frequencies (1) and (2) are completely attenuated by the first two-unit cells (which correspond to $d = 0.06p$). Higher attenuation is seen in (2) since the wave at this frequency does not propagate through any of the units. In the case of (3), the wave propagates through the first two units and then gets completely attenuated by the unit cells that correspond to $d = 0.08a$ and $d = 0.10p$, since its frequency lies in the overlapping region of the band gaps of $d = 0.08a$ and $d = 0.10p$. Finally, for the frequency indicated by (4), the wave propagates through the first four units, since it is no longer in the band-gap region associated with $d = 0.06p$ and $d = 0.08p$, but it gets completely reflected by the two units that correspond to $d = 0.10p$. For $p = 2$ cm, this hybrid sample would only be 6.5 cm in thickness but will facilitate an ultrawide band gap of width 130%.


[1] S. A. Cummer, J. Christensen, and A. Alù, Controlling sound with acoustic metamaterials, Nat. Rev. Mater. **1**, 16001 (2016).

[2] H. Ge, M. Yang, C. Ma, M.-H. Lu, Y.-F. Chen, N. Fang, and P. Sheng, Breaking the barriers: Advances in acoustic functional materials, Natl. Sci. Rev. **5**, 159 (2018).

[3] Y. Jin, Y. Pennec, B. Bonello, H. Honarvar, L. Dobrzynski, B. Djafari-Rouhani, and M. I. Hussein, Physics of surface vibrational resonances: Pillared phononic crystals, metamaterials, and metasurfaces, Rep. Prog. Phys. in press (2021).

[4] M. I. Hussein, M. J. Leamy, and M. Ruzzene, Dynamics of phononic materials and structures: Historical origins, recent progress, and future outlook, Appl. Mech. Rev. **66**, 040802 (2014).

[5] M. Oudich, Y. Li, B. M. Assouar, and Z. Hou, A sonic band Gap based on the locally resonant phononic plates with stubs, New J. Phys. **12**, 083049 (2010).

[6] F. Warmuth, M. Wormser, and C. Körner, Single phase 3D phononic band Gap material, Sci. Rep. **7**, 3843 (2017).

[7] O. McGee, H. Jiang, F. Qian, Z. Jia, L. Wang, H. Meng, D. Chronopoulos, Y. Chen, and L. Zuo, 3D printed architected hollow sphere foams with Low-frequency phononic band gaps, Addit. Manuf. **30**, 100842 (2019).

[8] X. Fei, L. Jin, X. Zhang, X. Li, and M. Lu, Three-Dimensional anti-chiral auxetic metamaterial with tunable phononic bandgap, Appl. Phys. Lett. **116**, 021902 (2020).

[9] F. Lucklum and M. J. Vellekoop, Bandgap engineering of three-dimensional phononic crystals in a simple cubic lattice, Appl. Phys. Lett. **113**, 201902 (2018).

[10] X. An, C. Lai, W. He, and H. Fan, Three-Dimensional meta-truss lattice composite structures with vibration isolation performance, Extreme Mech. Lett. **33**, 100577 (2019).

[11] S. Taniker and C. Yilmaz, Design, analysis and experimental investigation of three-dimensional structures with inertial amplification induced vibration stop bands, Int. J. Solids Struct. **72**, 88 (2015).

[12] K. H. Matlack, A. Bauhofer, S. Krödel, A. Palermo, and C. Daraio, Composite 3D-printed metastructures for low-frequency and broadband vibration absorption, Proc. Natl. Acad. Sci. U. S. A. **113**, 8386 (2016).

[13] W. Elmadih, D. Chronopoulos, W. P. Syam, I. Maskery, H. Meng, and R. K. Leach, Three-dimensional resonating metamaterials for low-frequency vibration attenuation, Sci. Rep. **9**, 11503 (2019).

[14] O. R. Bilal, D. Ballagi, and C. Daraio, Architected Lattices for Simultaneous Broadband Attenuation of Airborne Sound and Mechanical Vibrations in All Directions, Phys. Rev. Appl. **10**, 054060 (2018).

[15] L. D'Alessandro, E. Belloni, R. Ardito, F. Braghin, and A. Corigliano, Mechanical low-frequency filter via modes separation in 3D periodic structures, Appl. Phys. Lett. **111**, 231902 (2017).

[16] O. R. Bilal, A. Foehr, and C. Daraio, Observation of trampoline phenomena in 3D-printed metamaterial plates, Extreme Mech. Lett. **15**, 103 (2017).

[17] O. R. Bilal and M. I. Hussein, Trampoline metamaterial: Local resonance enhancement by springboards, Appl. Phys. Lett. **103**, 111901 (2013).

[18] Y. Jin, Y. Pennec, Y. Pan, and B. Djafari-Rouhani, Phononic crystal plate with hollow pillars connected by thin bars, J. Phys. Appl. Phys. **50**, 035301 (2016).

[19] X. Zheng, H. Lee, T. H. Weisgraber, M. Shusteff, J. DeOtte, E. B. Duoss, J. D. Kuntz, M. M. Biener, Q. Ge, J. A. Jackson, S. O. Kucheyev, N. X. Fang, and C. M. Spadaccini, Ultralight, ultrastiff mechanical metamaterials, Science **344**, 1373 (2014).

[20] A. Torrents, T. A. Schaedler, A. J. Jacobsen, W. B. Carter, and L. Valdevit, Characterization of nickel-based microlattice materials with structural hierarchy from the nanometer to the millimeter scale, Acta Mater. **60**, 3511 (2012).

[21] Q. Wang, J. A. Jackson, Q. Ge, J. B. Hopkins, C. M. Spadaccini, and N. X. Fang, Lightweight Mechanical Metamaterials with Tunable Negative Thermal Expansion, Phys. Rev. Lett. **117**, 175901 (2016).

[22] T. A. Schaedler, C. J. Ro, A. E. Sorensen, Z. Eckel, S. S. Yang, W. B. Carter, and A. J. Jacobsen, Designing metallic microlattices for energy absorber applications, Adv. Eng. Mater. **16**, 276 (2014).

[23] C. S. Ha, R. S. Lakes, and M. E. Plesha, Cubic negative stiffness lattice structure for energy absorption: Numerical and experimental studies, Int. J. Solids Struct. **178–179**, 127 (2019).

[24] M. Kadic, G. W. Milton, M. van Hecke, and M. Wegener, 3D metamaterials, Nat. Rev. Phys. **1**, 198 (2019).

[25] L. Cabras and M. Brun, A class of auxetic three-dimensional lattices, J. Mech. Phys. Solids **91**, 56 (2016).

[26] X. Ren, R. Das, P. Tran, T. D. Ngo, and Y. M. Xie, Auxetic metamaterials and structures: A review, Smart Mater. Struct. **27**, 023001 (2018).
[27] R. Lakes, Foam structures with a negative Poisson's ratio, Science **235**, 1038 (1987).
[28] M. Mir, M. N. Ali, J. Sami, and U. Ansari, Review of mechanics and applications of auxetic structures, Adv. Mater. Sci. Eng. **2014**, e753496 (2014).
[29] A. Spadoni, *An Isotropic Auxetic Structural Network with Limited Shear Stiffness* (American Society of Mechanical Engineers Digital Collection, Denver, Colorado, 2012), pp. 179–187.
[30] J. Dirrenberger, S. Forest, and D. Jeulin, Effective elastic properties of auxetic microstructures: Anisotropy and structural applications, Int. J. Mech. Mater. Des. **9**, 21 (2013).
[31] C. S. Ha, M. E. Plesha, and R. S. Lakes, Chiral three-dimensional isotropic lattices with negative Poisson's ratio, Phys. Status Solidi B **253**, 1243 (2016).
[32] J. N. Grima and K. E. Evans, Auxetic behavior from rotating squares, J. Mater. Sci. Lett. **19**, 1563 (2000).
[33] D. Attard and J. N. Grima, Auxetic behaviour from rotating rhombi, Phys. Status Solidi B **245**, 2395 (2008).
[34] J. N. Grima, L. Mizzi, K. M. Azzopardi, and R. Gatt, Auxetic perforated mechanical metamaterials with randomly oriented cuts, Adv. Mater. **28**, 385 (2016).
[35] J. Meng, Z. Deng, K. Zhang, X. Xu, and F. Wen, Band gap analysis of star-shaped honeycombs with varied Poisson's ratio, Smart Mater. Struct. **24**, 095011 (2015).
[36] A. Bacigalupo, M. Lepidi, G. Gnecco, and L. Gambarotta, Optimal design of auxetic hexachiral metamaterials with local resonators, Smart Mater. Struct. **25**, 054009 (2016).
[37] S. Mukherjee, Fabrizio Scarpa, and S. Gopalakrishnan, Phononic band gap design in honeycomb lattice with combinations of auxetic and conventional core, Smart Mater. Struct. **25**, 054011 (2016).
[38] L. D'Alessandro, V. Zega, R. Ardito, and A. Corigliano, 3D auxetic single material periodic structure with ultra-wide tunable bandgap, Sci. Rep. **8**, 2262 (2018).
[39] S. Krödel, T. Delpero, A. Bergamini, P. Ermanni, and D. M. Kochmann, 3D auxetic microlattices with independently controllable acoustic band gaps and quasi-static elastic moduli, Adv. Eng. Mater. **16**, 357 (2014).
[40] C. R. de Lima and G. H. Paulino, Auxetic structure design using compliant mechanisms: A topology optimization approach with polygonal finite elements, Adv. Eng. Softw. **129**, 69 (2019).
[41] T. A. Schaedler, A. J. Jacobsen, A. Torrents, A. E. Sorensen, J. Lian, J. R. Greer, L. Valdevit, and W. B. Carter, Ultralight metallic microlattices, Science **334**, 962 (2011).
[42] X. Zheng, W. Smith, J. Jackson, B. Moran, H. Cui, D. Chen, J. Ye, N. Fang, N. Rodriguez, T. Weisgraber, and C. M. Spadaccini, Multiscale metallic metamaterials, Nat. Mater. **15**, 1100 (2016).
[43] A. O. Krushynska, A. Amendola, F. Bosia, C. Daraio, N. M. Pugno, and F. Fraternali, Accordion-like metamaterials with tunable ultra-wide Low-frequency band gaps, New J. Phys. **20**, 073051 (2018).
[44] Y. Chen and L. Wang, Periodic co-continuous acoustic metamaterials with overlapping locally resonant and bragg band gaps, Appl. Phys. Lett. **105**, 191907 (2014).
[45] L. D'Alessandro, E. Belloni, R. Ardito, A. Corigliano, and F. Braghin, Modeling and experimental verification of an ultra-wide bandgap in 3D phononic crystal, Appl. Phys. Lett. **109**, 221907 (2016).
[46] M. Oudich, B. Djafari-Rouhani, Y. Pennec, M. B. Assouar, and B. Bonello, Negative effective mass density of acoustic metamaterial plate decorated with low frequency resonant pillars, J. Appl. Phys. **116**, 184504 (2014).
[47] Y. Lai, Y. Wu, P. Sheng, and Z.-Q. Zhang, Hybrid elastic solids, Nat. Mater. **10**, 620 (2011).
[48] X. Zhang and Z. Liu, Negative refraction of acoustic waves in two-dimensional phononic crystals, Appl. Phys. Lett. **85**, 341 (2004).
[49] X. Zhou, M. B. Assouar, and M. Oudich, Acoustic superfocusing by solid phononic crystals, Appl. Phys. Lett. **105**, 233506 (2014).
[50] D. Chen and X. Zheng, Multi-material additive manufacturing of metamaterials with giant, tailorable negative Poisson's ratios, Sci. Rep. **8**, 9139 (2018).
[51] G. Imbalzano, P. Tran, T. D. Ngo, and P. V. Lee, Three-dimensional modelling of auxetic sandwich panels for localised impact resistance, J. Sandw. Struct. Mater. **19**, 291 (2017).
[52] N. J. Gerard, H. Cui, C. Shen, Y. Xie, S. Cummer, X. Zheng, and Y. Jing, Fabrication and experimental demonstration of a hybrid resonant acoustic gradient index metasurface at 40 KHz, Appl. Phys. Lett. **114**, 231902 (2019).
[53] See Supplemental Material at http://link.aps.org/supplemental/10.1103/PhysRevApplied.16.024015 for animations of the mode shapes, and of the elastic wave propagating through the elastic metamaterial in three different crystalline orientations.